Deepening the scientific understanding of different phenomenology in laser powder bed fusion by an integrated framework

Liping Guo [a,b], Hanjie Liu [a,b], Hongze Wang [a,b,c,*], Valentino A.M. Cristino [d], C.T. Kwok [d], Qianglong Wei [a,b], Zijue Tang [a,b], Yi Wu [a,b,c,*], Haowei Wang [a,b,c,e]

[a] *State Key Laboratory of Metal Matrix Composites, Shanghai Jiao Tong University, Shanghai, 200240, China*
[b] *School of Materials Science & Engineering, Shanghai Jiao Tong University, Shanghai, 200240, China*
[c] *Institute of Alumics Materials, Shanghai Jiao Tong University (Anhui), Huaibei, 235000, China*
[d] *Department of Electromechanical Engineering, University of Macau, Avenida da Universidade, Taipa, Macao*
[e] *Anhui Province Industrial Generic Technology Research Center for Alumics Materials, Huaibei Normal University, Huaibei, 235000, China*

ARTICLE INFO

ABSTRACT

Additive manufacturing technology has greatly improved the design flexibility and accelerated the optimization verification of structure that cannot be easily and economically produced by traditional subtractive manufacturing processes. However, common defects such as surface roughness and porosity, affect the quality and reliability of the components, hindering their wide application. In this study, an integrated framework incorporating high-fidelity powder-scale mechanistic model and physics-informed machine learning is developed to predict the built quality of aluminum and to determine the hierarchy importance of mechanistic variables for different printing qualities in a multi-classification problem in the processing space. The influence of different processing parameters on the built quality is explored by the mechanistic model. A decision tree is constructed and the quality prediction index (QPI) connecting five variables and the printing quality is established. The hierarchy importance of the mechanistic variables is determined by the QPI and three machine learning inductions. The most important factor for balling, good printing quality, keyhole and lack of fusion defects are *Fo, TP, fr* and *Tp*, respectively. As the mechanistic variable values are the comprehensive results of multiple processing parameters, this hierarchy ranking not only deepens the scientific understanding of different phenomenology, but also provides new insights and strategies for the process optimization.

1. Introduction

Additive manufacturing (AM) technology that produces parts layer by layer from a three-dimensional computer-aided design model is a potentially disruptive technology among many industries [1,2]. The process provides the extreme flexibility of design and fabricating fine structures compared to the traditional subtractive manufacturing processes [3,4]. Among the many AM technologies, laser powder bed fusion (LPBF) is the most typical and adopted method for the manufacturing of metallic components [5].

The suitability to produce components by LPBF depends on two aspects, described in terms of printability, which is considered to be a global indicator of the resistance to micro/macro defect formation that compromises the part integrity for an alloy-process combination [6]. (i) One is the intrinsic factors that affect the microstructure, including the range of solidification, secondary phase, etc. [7–12]; (ii) The other aspect is extrinsic processing factors that affect the overall consistency of the printed parts [13–16]. The printing quality of LPBF manufactured parts is affected by more than 130 processing parameters, among which the most commonly investigated are laser power, scanning speed, hatching distance, layer thickness and preheating temperature [17–21]. The common defects found in parts are porosity and surface roughness, which formation are governed by the complex relationship between high-velocity vapor, powder movement and molten pool dynamics, and can be detrimental to structural integrity and mechanical performance, leading to the premature failure [22–26]. AM research has been largely focused on studies to deepen the knowledge of the process by understanding and finding useful combinations of these external factors.

So far, many researchers have studied the printability from the perspective of molten pool characteristics as many phenomena and defects occur at the molten pool scale, both the time and spatial scale [27,

---

* Corresponding authors.
E-mail addresses: hz.wang@sjtu.edu.cn (H. Wang), eagle51@sjtu.edu.cn (Y. Wu).

Nomenclature

d:	depth of molten pool	μ:	viscosity
t:	powder layer thickness	g:	gravitational acceleration
l:	length of molten pool	U_g:	velocity of shielding gas
$w1$:	width of molten pool from the top view	U_l:	maximum fluid convective velocity
$w2$:	width of the molten pool on the upper surface of substrate	Tp:	dimensionless peak temperature
α:	thermal diffusivity	Fo:	Fourier number
V:	scanning speed	Ma:	Marangoni number
P:	laser power	td:	solidification time
T:	temperature	R:	Richardson number
p:	pressure	fr:	ratio of recoil pressure and surface tension
Fd:	drag force coefficient	$\vec{v}$:	velocity vector
$\vec{n}$:	surface normal vector	h:	enthalpy
h_c:	heat transfer coefficient	k:	thermal conductivity
σ:	Stefan-Boltzmann constant	F:	volume of the fluid
ε:	radiation emissivity	q:	laser heat flux
		t_s:	time

28]. By combing the *in-situ* thermal imaging and *ex-situ* characterization, Scime et al. [29] developed a method to map the molten pool defects to the laser power and scanning speed, and related such defect occurrence to the major features of the molten pool geometry. Zhao et al. [30] identified the keyhole porosity boundary in the power-scanning speed map by using high-speed X-ray imaging, which separated the processing parameters for fabricating nominally fully dense parts from those with pores. *In-situ* imaging techniques offer a unique ability to observe the molten pool without interfering the experimental producers [31–33]. They are very challenging and expensive due to the high temporal and spatial resolution required, as well as massive data processing for identifying the process window. Numerical simulation has the potential to be a viable and cost-effective alternative to address the challenge and is increasingly used to study the molten pool dynamics, which can also provide unique insights into molten pool evolution and defect formation mechanisms, as well as solutions for process optimization [34–37]. Wu et al. [38] attributed the spattering to the high momentum of the molten metal, high recoil pressure, shear force and low surface tension by computational fluid dynamics modeling. Papazoglou et al. [39] demonstrated that balling is resulted from the energy density and Plateau-Rayleigh capillary instability. Panwisawas et al. [40] established the additive manufacturability map based on the porosity, cooling rate and volatile mass loss by a multiphysics model. Johnson et al. [6] proposed a printability metric for LPBF by a finite element thermal model, which is defined as the volume in the laser power-scanning speed space.

In a multi-variable process, the impact of individual processing variable on the part quality is often concealed by the influence of other variables and the complexity of the process, making it difficult to uncover the hierarchy of the important variables. Moreover, the mapping relations between raw variables and final quality cannot provide an in-depth understanding of the physics behind the phenomenon. Therefore, more and more researchers have sought to the combination of numerical simulation with data-driven machine learning techniques via several mechanistic variables that embodies the effects of alloy properties and processing parameters, making calculations tractable [41–45]. For example, Du et al. [43] proposed a quantitative framework to uncover the mechanism of balling defects in AM by combining the physics-informed machine learning, mechanistic model and peer-reviewed experimental data. Six important causing variables were identified, which were calculated and then used in machine learning to obtain the hierarchical importance of defect formation variables. They also used multiple machine learning algorithms and numerical simulations to identify the mechanistic variables leading to friction stir welding tool failure, and the maximum shear stress was determined to be the

dominate cause [46]. Jiang et al. [42] implemented the augmented machine learning strategy and a mechanistic model, as well as historical experimental data to explore the conditions for reducing the lack of fusion (LOF) voids in LPBF, and the hierarchical influence of the five important variables on the LOF defects was uncovered. A similar approach was adopted by Mondal et al. [41] to investigate cracking in AM parts. The effects of five variables related to the physics of cracking were evaluated and a cracking susceptibility index to predict crack formation before printing was established. But in their mechanistic models, the free surface evolution and the randomly packed powder bed are not included, which will affect the calculation results, such as the thermal history, molten pool dynamics and morphology. Besides, till now, the relationships between the multiple processing variables, multiple mechanistic variables, and printing quality in a multi-classification problem involving in the processing space have not been reported.

In this work, the quality prediction index (QPI) is established to predict the built quality of aluminum based on a comprehensive framework containing high-fidelity powder-scale mechanistic model and physics-informed machine learning in a multi-classification problem in the processing space. The influence of different processing variables on the printing quality is explored. Five mechanistic variables are determined and calculated by the mechanistic model. The solidified track quality is predicted, and the hierarchical importance of mechanistic variables is explored by different machine learning algorithms, which will greatly promote the scientific understanding behind different track phenomena and provide a framework for the selection of printing parameters.

2. Methodology

LOF occurs when the incident laser energy is insufficient to melt the substrate to a significant depth, which can result in large or very sharp voids within the built part [47,48]. When the molten pool is unstable with a large aspect ratio, balling occurs under Kelvin–Helmholtz instability or Plateau-Rayleigh instability, increasing the surface roughness and even affecting the powder spreading during the subsequent layer processing [49,50]. Intensive evaporation and depression take place under huge heat input, which will lead to compositional inhomogeneity and even porosity [35,51]. According to the literature in this field [6,29, 52], the built qualities can be classified by molten pool characteristics, including LOF, balling and keyhole. The classification thresholds for the formation of the above three phenomena are $d/t < 0.5$, $l/w1 > 2.1$, and $d/w2 > 0.45$, respectively. Among them d represents the molten pool depth, t is powder layer thickness, l is the molten pool length, $w1$ is the molten pool width from the top view and $w2$ is the width on the upper

surface of substrate, respectively. The corresponding good type is the remaining region after eliminating the regions corresponding to the above-mentioned three types of phenomena in the processing space.

2.1. Physics-informed machine learning

In a complex system like LPBF process, there are a vast range of processing parameters that affect the overall quality of the manufactured parts, and most research has mainly focused on finding useful combinations of these external factors to obtain better printing quality. The use of data-driven machine learning techniques can establish the relationships between different processing parameters and built quality, in which raw variables are the most convenient input as they can be easily obtained directly during the experiment. Furthermore, engineers can easily control these variables to achieve desired product properties. However, the influence of single parameter will be affected by the complex interdependence of the many processing variables, and the in-depth understanding physics and the roles of the raw variables in part quality cannot be easily obtained and analyzed. Based on the wide knowledge on metallurgy and mechanisms of various phenomena, the

combination of numerical simulation with data-driven machine learning through mechanistic variables provides a good solution for the problem above, which can significantly reduce the amount of trial-and-error based experimental data. These mechanistic variables can also be called "causing variables" as they provide the insights on the physical mechanisms behind the phenomena, which embody the effects of alloy properties and processing parameters.

The methodology overview of this work is presented in Fig. 1, including three essential components: LPBF process, mechanistic model and machine learning. The raw variables are used in the mechanistic model to determine the built quality in terms of the molten pool morphology, and to calculate the mechanistic variables (dimensionless peak temperature, Richardson number, ratio of recoil pressure and surface tension, solidification time and Fourier number). These mechanistic variables used in machine learning can predict the built quality, and will assist in the optimization of LPBF processes and reduce common defects such as balling, porosity and surface roughness.
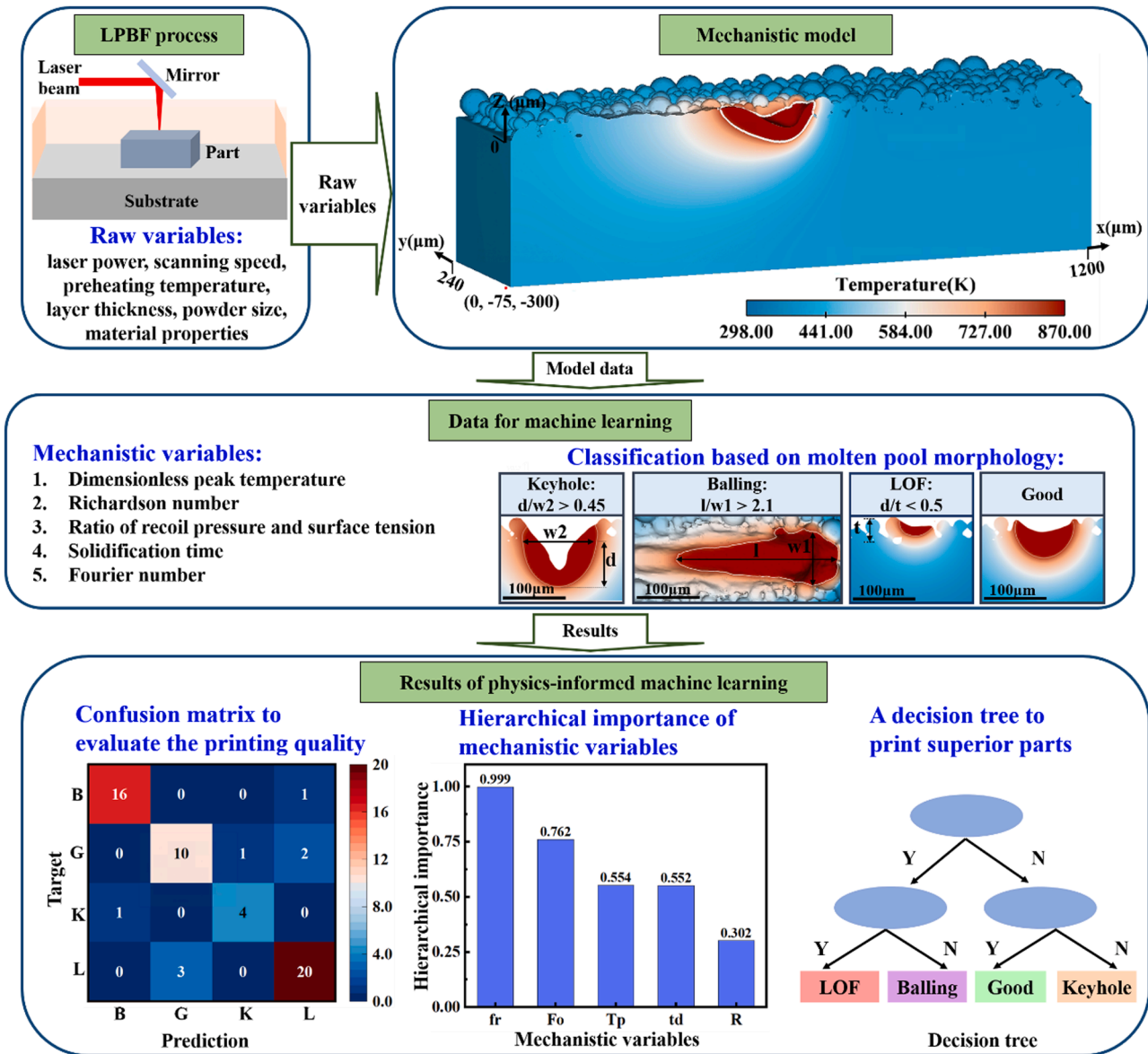

Fig. 1. Overview schematic of the approach proposed and used in this work. The axis labelled as 'Prediction' represents the predicted output of the machine learning. 'B', 'G', 'K', and 'L' represent balling, good, keyhole and LOF, respectively.

2.2. Modeling

The powder bed is generated via the commercial software Particle Flow Code (PFC). The high-fidelity computational fluid dynamics (CFD) model is established using the commercial software Flow 3d, shown in the upper right corner of Fig. 1. And the model has been well validated in our previous work [4,53]. The dimensions of the computational domain is $1200 \times 480 \times 400\ \mu m^3$ (length × width × height), with a mesh size of 4 μm. The thermophysical and mechanical properties of the materials used in this simulation can be found in ref. [4]. The thermal history, molten pool dynamics and the evolution of the free surface can be obtained by solving conservation equations, shown in Eqs. (1)–(4).

$$\nabla \cdot (\overrightarrow{v}) = 0 \tag{1}$$

$$\frac{\partial \overrightarrow{v}}{\partial t} + \overrightarrow{v} \cdot \nabla \overrightarrow{v} = -\frac{1}{\rho}\nabla p + \mu \nabla^2 \overrightarrow{v} - F_d \overrightarrow{v} + \overrightarrow{G} \tag{2}$$

$$\rho \left[\frac{\partial h}{\partial t} + (\overrightarrow{v} \cdot \nabla)h \right] = \nabla \cdot (k\nabla T) \tag{3}$$
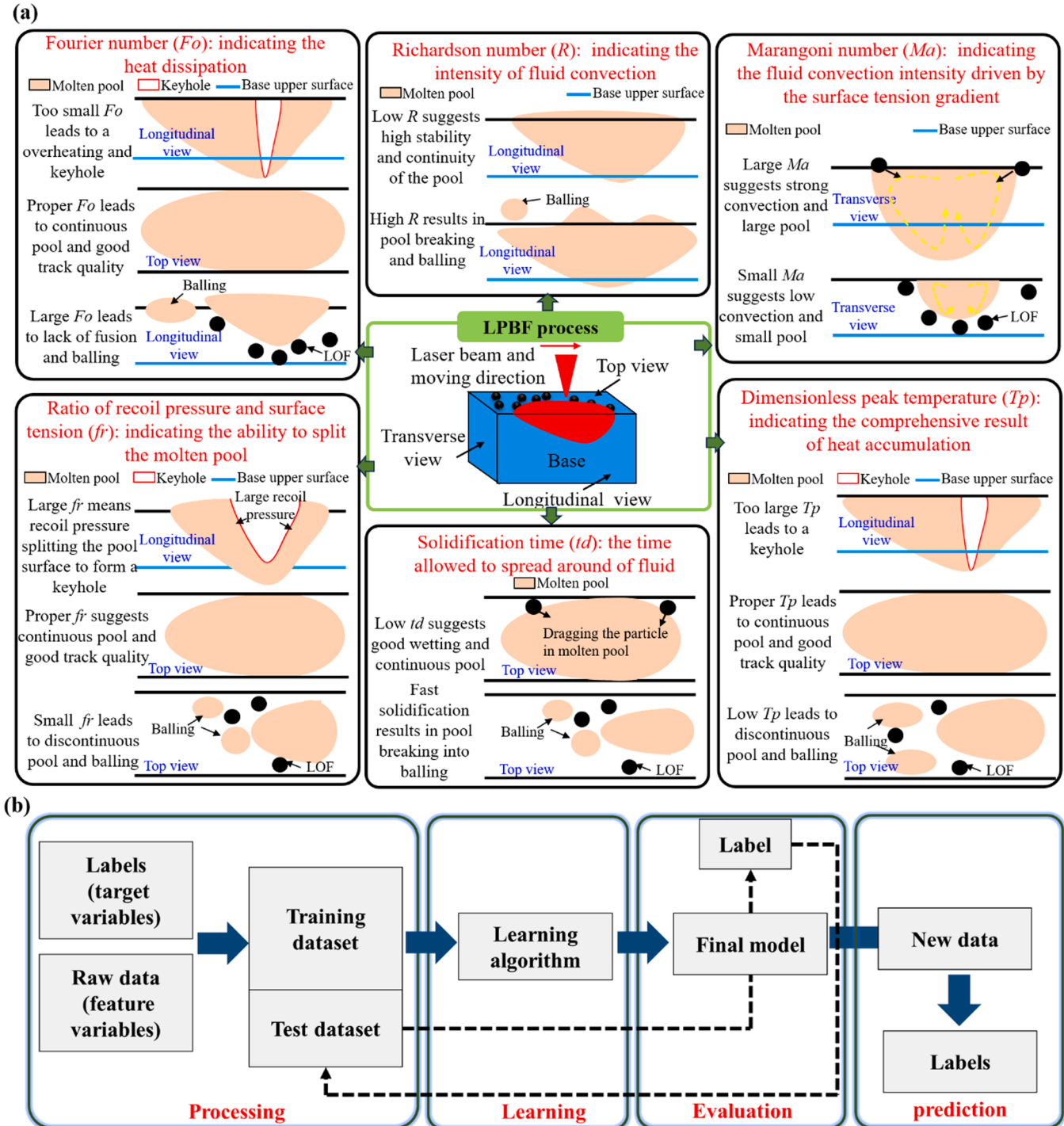

Fig. 2. (a) Schematic to illustrate the effects of the mechanistic variables on the balling, keyhole and LOF defects. The subfigure in the center shows the schematic of LPBF process and different views. (b) Flowchart of the machine learning.

$$\frac{\partial F}{\partial t} + \nabla \cdot \left(\vec{v} F \right) = 0 \qquad (4)$$

here $\vec{v}$ (m·s^{-1}) is the velocity vector. t (s) is the time, ρ (kg·m^{-3}) is the density, p (Pa) is the pressure and μ (m^2·s^{-1}) is the kinematic viscosity. F_d (s^{-1}) is the drag force coefficient. $\vec{G}$ (m·s^{-2}) is the body acceleration due to body force. h (J·kg^{-1}) is the enthalpy, k (W· m^{-1}·K^{-1}) is the thermal conductivity and T (K) is the temperature. F is the volume of the fluid.

The laser heat source is regarded as a part of the surface heat flux boundary condition, The main energy transfer modes in the upper free surface include convection, radiation and evaporation, expressed as:

$$k\frac{\partial T}{\partial \vec{n}} = q - q_{conv} - q_{rad} - q_{evap} \qquad (5)$$

$$q_{conv} = h_c \left(T - T_{ref} \right) \qquad (6)$$

$$q_{rad} = \sigma\varepsilon \left(T^4 - T_{ref}^4 \right) \qquad (7)$$

$$q_{evap} = \varphi L_v P_{atm} \sqrt{\frac{1}{2\pi RT}} exp\left[\frac{L_v(T - T_b)}{TRT_b} \right] \qquad (8)$$

here q (J·m^{-2}·s^{-1}) is the laser heat flux absorbed by the free surface, $\vec{n}$ is the surface normal vector and h_c (W· m^{-2}·K^{-1}) is the heat transfer coefficient. σ (W· m^{-2}·K^{-4}) is the Stefan-Boltzmann constant and ε is the radiation emissivity. For other surfaces, only convection and radiation are considered.

$$k\frac{\partial T}{\partial \vec{n}} = -q_{conv} - q_{rad} \qquad (9)$$

2.3. Calculation of mechanistic variables based on multi-physics model

The occurrence of different phenomena is mainly related to the heat transfer and fluid flow in the molten pool. Based on the knowledge on metallurgy and mechanisms behind various phenomena, six mechanistic variables were initially selected to represent the comprehensive impact of processing variables on the solidified track quality, which includes dimensionless peak temperature (Tp), Fourier number (Fo), Marangoni number (Ma), solidification time (td), Richardson number (R), and ratio of recoil pressure and surface tension (fr). The scientific basis for choosing these causing variables is discussed in the following paragraphs and illustrated in the schematic in Fig. 2(a).

Dimensionless peak temperature (Tp). The transient temperature field is an important prerequisite for the mechanism research during the interaction of laser-matter. A dimensionless number Tp is defined as the ratio of the peak temperature in the molten pool to the liquid temperature of the alloy, which reflects the heat absorption and tells the state of the molten pool. A low Tp means insufficient heat input, leading to discontinuous molten pool and lack of fusion defects. A proper Tp is an indirect indicator of a continuous and large molten pool. In this case, the molten pool can penetrate deeply into the substrate, and adjacent tracks can form successful bonding, which is conducive to the formation of good tracks [42]. Too large Tp value suggests the peak temperature much higher than the boiling point, and serious evaporation will occur according to the Clausius–Clapeyron relation, leading to the composition inhomogeneity and formation of keyhole, or even a keyhole pore. Therefore, Tp can be an indicator of the built quality.

Fourier number (Fo). The heat conduction and storage will have an influence on the molten pool state and dynamics, as well as the final built quality. The heat conduction and dissipation can be described by a dimensionless quantity Fo. Its physical meaning is the ratio of heat conduction or diffusion rate to heat storage rate. A high Fo indicates the faster heat dissipation and smaller heat storage, increasing the

vulnerability to balling and LOF defects. A small Fo is favorable of continuous molten pool and good built quality. However, too small Fo may lead to heat accumulation and overheating, resulting in keyhole phenomenon. Therefore, Fo can be an indicator of the built quality. It is defined as:

$$Fo = \alpha/Vl \qquad (10)$$

where α (m^2·s^{-1}) is the thermal diffusivity, V (m·s^{-1}) is the scanning speed. The molten pool length can be calculated by a mechanistic model.

Marangoni number (Ma). The molten pool shape and dimensions are largely influenced by the inside fluid convection, which is mainly driven by the surface tension gradient on the top of the molten pool, can be characterized by the Ma. A higher Ma indicates a stronger convective flow, which is beneficial for the fluid to diffuse evenly and maintaining the continuity of the molten pool. It will also increase the molten pool dimensions, improve the remelting and bonding with adjacent tracks, and reduce LOF defects. The Ma is expressed as:

$$Ma = -\frac{d\gamma}{dT}\frac{w1\Delta T}{\mu\alpha} \qquad (11)$$

in which $\frac{d\gamma}{dT}$ is the surface tension gradient, $w1$ (m) and μ (kg·m^{-1}·s^{-1}) are the molten pool width on the top surface and viscosity, respectively. ΔT (K) is the temperature difference between the peak temperature inside molten pool and the solidus temperature of the alloy, which can be calculated by a mechanistic model.

Solidification time (td). The liquid existing time which allows the molten metal to spread, and wet the powder and substrate, will significantly affect the built quality. For example, under the condition of rapid solidification, the fluid cannot spread evenly, and the molten pool breaks into isolated balls and forms discontinuous tracks, which will increase the surface roughness and the vulnerability to void formation. The solidification time of the molten pool can be determined by the ratio of the molten pool length to the scanning speed.

Richardson number (R). Balling or hump may form due to the molten pool segregation under the effect of Helmholtz instability or Plateau-Rayleigh instability [25,39], which is caused by the velocity difference between the shielding gas and the fluid convection at the top surface of the molten pool. This hydrodynamic instability can be characterized by the dimensionless R. Due to the high instability of the molten pool, the sensitivity to balling defects increases with R, and it can be calculated by:

$$R = \frac{gl}{\left(U_g - U_l \right)^2} \qquad (12)$$

where g (m·s^{-2}) is the gravitational acceleration, U_g (m·s^{-1}) is the velocity of shielding gas and is assumed to be the scanning speed, and U_l (m·s^{-1}) is the maximum fluid convective velocity, which can be obtained by the mechanistic model.

Ratio of recoil pressure and surface tension (fr). Surface tension maintains the integrity of the molten pool, while the recoil pressure is the driving force for the fluid separation to generate the depression at the top surface of the molten pool under high heat input. When the heat input is extremely low and evaporation does not occur, the surface tension is the main driving force to keep the track integrity. For the cases with high heat input, the temperature in the molten pool will exceed the boiling point of the alloy, decreasing the surface tension but increasing the recoil pressure exponentially [54,55], and a keyhole may be formed. Therefore, the ratio of recoil pressure and surface tension can be used to indirectly characterize the different track phenomena. The surface tension is the product of the surface tension coefficient of the alloy and the perimeter of the molten pool on the top surface. The molten pool perimeter and the recoil pressure can be calculated by the mechanistic model.

2.4. Implementation of machine learning and data used in the analysis

The purpose of machine learning is to find the mapping relationship between feature variables and target variables, and then realize the prediction. The standard flowchart of machine learning is shown in Fig. 2(b). In this work, the feature variables are those mechanistic variables which can be obtained according to the definition equations, in which the unknown variables such as temperature, velocity, force et al. are the calculation results of the heat transfer and fluid flow model. They are the input data of the machine learning. The labels including four kinds of built quality (LOF, balling, good and keyhole) based on the molten pool morphology are the output results. The machine learning analysis is based on 58 data points, and each data point corresponds to a different combination of mechanistic variables and the final printing quality. Among the many machine learning algorithms, decision tree (DT) model shows great superiority for data-classifying problems. Support vector machine (SVM) is useful for solving non-linear and high-dimensional classification problems and establishing a relationship between the input and output based on a function, as well as predicting for a set of input parameters. While the logistic regression (LR) can give an algebraic equation correlating the feature variables and the target variables, and reveal the hierarchy importance of the feature variables. Here, these three algorithms are adopted to predict the built quality of a single track and establish a relationship between the mechanistic variables and the built quality, as well we determine the hierarchy importance of the mechanistic variables. The range of processing parameters and mechanistic variables for all data are shown in Table 1. The processing parameters and mechanistic variables for all cases are given in the Supplementary information in table s1. As the data point is small, the 13-fold cross-validation method is utilized to improve the prediction robustness.

The hierarchy importance of the mechanistic variables on the built quality is based on three feature selection indexes: (i) information gain, (ii) information gain ratio and (iii) Gini index, which are calculated by the three commonly used machine learning algorithms ID 3, C4.5 and CART, respectively. As the information gain and information gain ratio are computed from the entropy, a higher value indicates a higher importance of the mechanistic variable. While the Gini index is calculated based on the impurity, thus, a more important mechanistic variable will present a smaller Gini index. The method for computing the three indexes is described in Supplementary Information. A decision tree is created based on the CART algorithm to provide a qualitative tool to predict built quality, and the mechanistic variable with the lowest Gini value is selected as the root node. The tree contains multiple nodes and each node corresponds to a mechanistic variable. The data is split according to the threshold until the rest data belongs to the same category.

2.5. Experiment

The powder material used in this study is TB-AlSi10Mg (6 wt% TiB₂-AlSi10Mg), and fabricated by gas atomization. To explore the effects of powder sizes on the surface roughness, the single layer experiments are conducted on the machine Prox DMP 200 (3D system, USA), which is equipped with a maximum laser output power of 300 W, a wavelength of 1070 nm and a focused laser beam diameter of 75 µm. Two different sizes of powder with $D_{50} = 15.60$ µm and 39.22 µm are investigated. The powder bed thickness is 30 µm. The detailed fabrication process can be referred in Ref. [4,56].

3. Results and discussion

The effects of different preheating temperatures, powder layer thickness and powder size on the printing quality are evaluated in this section. As the mapping relationship between raw variables and the final built quality cannot reveal the corresponding physics behind the phenomenon, five mechanistic variables for physics-informed machine learning are finally determined via Pearson correlation analysis for the multiple classification problem. The index for different phenomena is established by logistic regression, and the hierarchy importance of the mechanistic variables are determined by the feature selection indexes of ID 3, C4.5 and CART algorithms.

3.1. Effects of processing parameters on the molten pool characteristic

In this section, the influence of different processing parameters on the built quality is explored.

3.1.1. Preheating temperature

The effects of preheating temperature on the molten pool characteristic are shown in Fig. 3, in which the ratio of molten pool depth to powder thickness, the ratio of molten pool length to width, and the ratio of molten pool depth to width are the indicators of LOF, balling and keyhole, respectively. For the case of 225 W-1400 mm·s⁻¹, it belongs to LOF category at room temperature (300 K), and with the increase of preheating temperature (300 K→500 K), it gradually changes to the good category. The solidified track height also increases with the increase of the preheating temperature, which can be attributed to that a higher temperature leads to increased melting degree of the powder (increased molten metal flux). While the standard deviation decreases as the temperature increases, indicating that for the LOF condition, a reasonable preheating can obtain a smoother surface. For the processing parameters of 300 W-1800 mm·s⁻¹, they all belong to balling judged by the clarification criterion. The aspect ratio of the molten pool and the standard deviation of the solidified track height increase with the increase of the preheating temperature, indicating that the balling is more and more evident. Or in other words, for the case of balling under room temperature, it becomes more pronounced as the preheating temperature increases.

The effects of preheating temperatures on the porosity and solidified track quality can be observed in Fig. 4. For the printing parameter which causes LOF defects at ambient temperature, the increase of preheating temperature can effectively lower the porosity. While for the printing parameter that balling occurs at room temperature, the surface fluctuations of the solidified track become severer with increased temperature.

Based on the classification criterion on the basis of molten pool morphology, the roles of raw processing parameters in determining the final quality can be obtained, but the physics behind different phenomena is not clear. Preheating will change the heat accumulation in the molten pool. The LOF phenomenon corresponds to low heat input and small molten pool, and balling is due to the instability of the molten pool, which is related to fluid flow. Therefore, an attempt is made to analyze the physical mechanism of the influence of preheating on the characteristics of the molten pool through *Tp* and *Ma*, which measures the fluid flow intensity, shown in Fig. 5.

For the case of 225 W-1400 mm·s⁻¹ categorized into LOF, it can be observed that as the preheating temperature increases, the *Tp* of the

Table 1
Range of processing parameters and mechanistic variables.

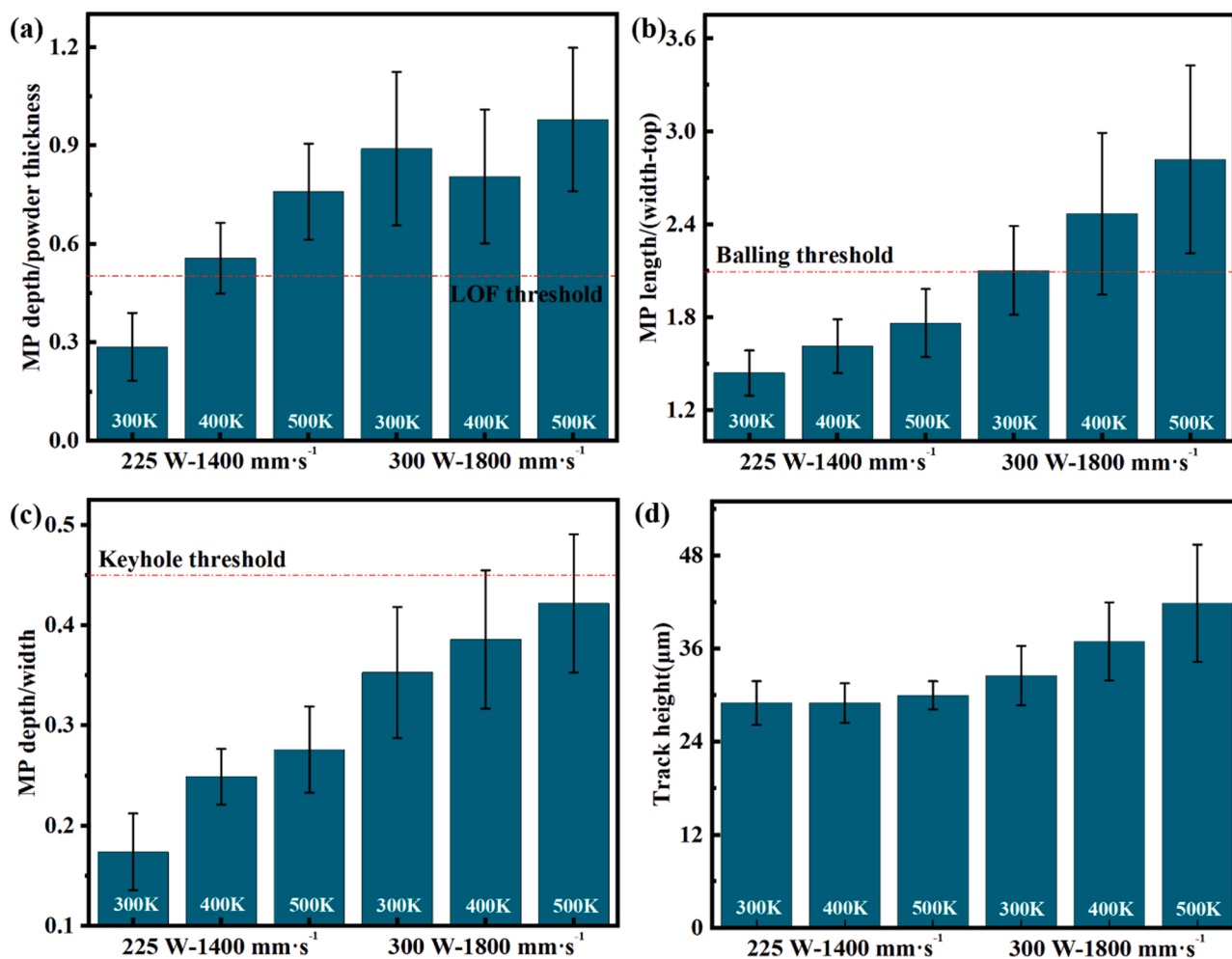| Raw variables	Range	Causing variables	Range
Laser power (W)	90 – 600	Fourier number	0.040 – 1.06
Scanning speed (mm·s⁻¹)	600 – 4000	dimensionless peak temperature	1.85 – 4.65
Preheating temperature (K)	300, 400, 500	Ratio of recoil pressure and surface tension	0 – 127.77
Layer thickness (µm)	0, 25, 30, 40	Marangoni number	185 – 2120
Powder size, D₅₀ (µm)	33, 41	Richardson number	2.93E-5 – 1.4E-4
		Solidification time (s)	2.8E-5 – 2.9E-4

Fig. 3. The effects of different preheating temperatures on the molten pool characteristics, (a) ratio of molten pool depth to powder thickness, (b) ratio of molten pool length to width, (c) ratio of molten pool depth to width, and (d) solidified track height. The powder thickness is 30 μm, and the powder size of $D_{50} = 33$ μm. The dotted lines in (a) – (c) indicate that the corresponding phenomenon occurs when the characteristic value of the molten pool is higher or lower than the threshold.

molten pool also increases, resulting in larger melting degree of the powder and the larger molten pool. The *Ma* indicates the degree of fluid flow in the molten pool, in which a higher *Ma* means a stronger convective flow, resulting in the fluid diffusing evenly and a larger molten pool, weakening the LOF defects. It is apparent from Fig. 5 that *Ma* increases with the increasing of the preheating temperature, indicating a strong fluid flow, which is more favorable to fluid spreading and filling the LOF voids, leading to the change from LOF to good. For the case of 300 W-2200 mm·s⁻¹, the *Tp* decreases as the preheating temperature increases, which can be attributed to that higher preheating temperature causes more intense evaporation and greater the heat loss. However, the results in Fig. 3 show that with the increase of preheating temperature, the molten pool dimension increases instead, which implies that the complex dynamics in the molten pool cannot be characterized only by the peak temperature. The dimensionless analysis reveals that *Ma* increases with a higher preheating temperature, indicating that the fluid flow in the molten pool is more intense, resulting in the larger molten pool and more pronounced balling phenomenon.

3.1.2. Powder size

The powder size is also an important variable in the LPBF process as it affects the powder flow, heat absorption in the molten pool and thus impacts the built quality [57,58]. Here, two different sizes of powder with $D_{50} = 33$ μm and 41 μm are simulated to explore their effects on the molten pool characteristics and solidified track height, which is a

response of the surface quality, as shown in Fig. 6. The aspect ratio of the molten pool indicates the stability of the molten pool, where a larger value means a higher vulnerability to balling. It can be seen from Fig. 6 that the larger the powder particle size, the larger will be the aspect ratio of the molten pool. Moreover, for the balling phenomenon, a larger standard deviation of the solidified track height means a more serious surface fluctuation, indicating the more significant balling. The results in Fig. 6 show that the standard deviations for the powder with $D_{50} = 41$ μm are larger than those of the powder with $D_{50} = 33$ μm, indicating that a larger particle size increases the vulnerability to balling. Our experimental results in Fig. 7 uncover that the surface roughness increases with the increase of scanning speed, which can be attributed to that higher speed results in lower melting degree. Besides, it also reveals that the surface built with larger particles possesses higher surface roughness. Therefore, it can be inferred that under the reasonable heat input, small powder can assist in better quality prints.

3.1.3. Layer thickness

The powder layer thickness is an important variable in the LPBF process, as thin powder bed will lower the printing efficiency, while a thicker layer of powder will require greater heat input to make sure the molten pool penetrating into the substrate to form a good bonding. Based on the above discussion, balling phenomenon occurs under the printing parameter of 300 W-2200 mm·s⁻¹ with a layer thickness of 30 μm. Therefore, in order to obtain an apparent surface phenomenon, this
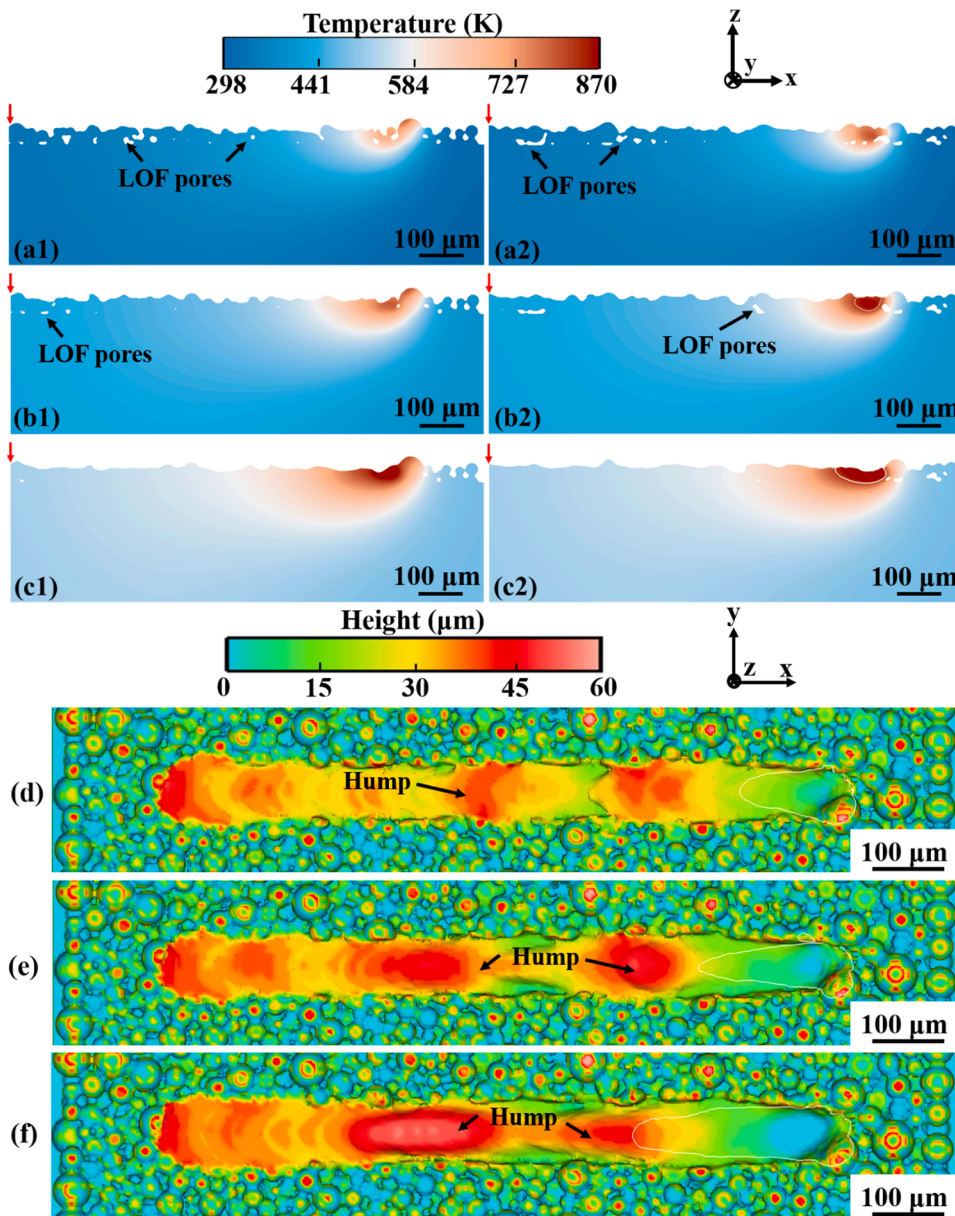
Fig. 4. Effects of different preheating temperatures on LOF voids, (a1) (a2) 300 K, (b1) (b2) 400 K and (c1) (c2) 500 K with the power-scanning speed combination of 225 W-1400 mm·s^{-1}. Effects of different preheating temperatures on balling formation, (d) 300 K, (e) 400 K and (f) 500 K with the power-scanning speed combination of 300 W- 2200 mm·s^{-1}. The red arrows show the initial position of the laser and the solid white lines indeicate the solidus line. (a1)-(c1) are the cross-sections at $y = -115$ μm, and (a2)-(c2) are the cross-sections at $y = -35$ μm. The laser moves along the line of $y = -75$ μm towards the positive of x-axis.
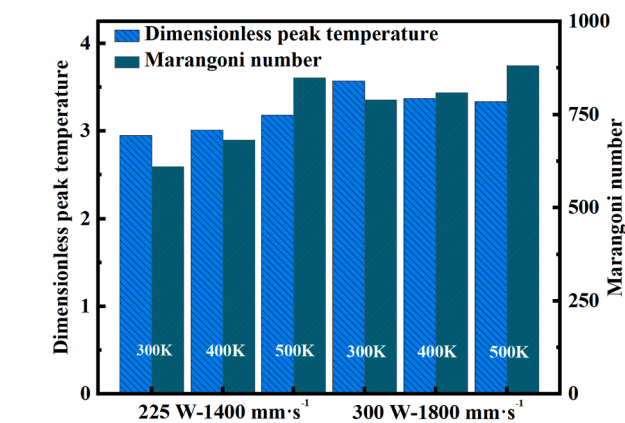
Fig. 5. Effects of different printing parameters on the dimensionless temperature and Marangoni number. Considering the dynamic change of the molten pool, the peak temperature is an average of the peak temperatures extracted every 20 μs.

power-scanning speed combination is used to explore the effects of different layer thicknesses on the molten pool characteristics and the solidified track height. Fig. 8 shows that the molten pool aspect ratio decreases with the increase of layer thickness, and the balling effect weakens, which gradually turns to LOF instead. When the layer thickness is 40 μm, the large standard deviation of the track height is due to the incompletely melted powder, because a thick powder layer lowers the effective heat transfer efficiency, causing low melting degree and small molten pool, resulting in severe surface fluctuations [59,60]. This also indicates that under the same heat input, the thinner powder layer leads to more unstable molten pool, which is prone to balling/hump. In practice, increasing the layer thickness can improve the efficiency, but a layer too thick will lead to incomplete melting. Therefore, it is necessary to find a balance between printing efficiency and printing quality.

3.2. Printability prediction using physics-informed machine learning

The combination of numerical simulation and physics-informed machine learning will provide a better understanding on the physics of the different phenomena in a multi-variables process. The choice of
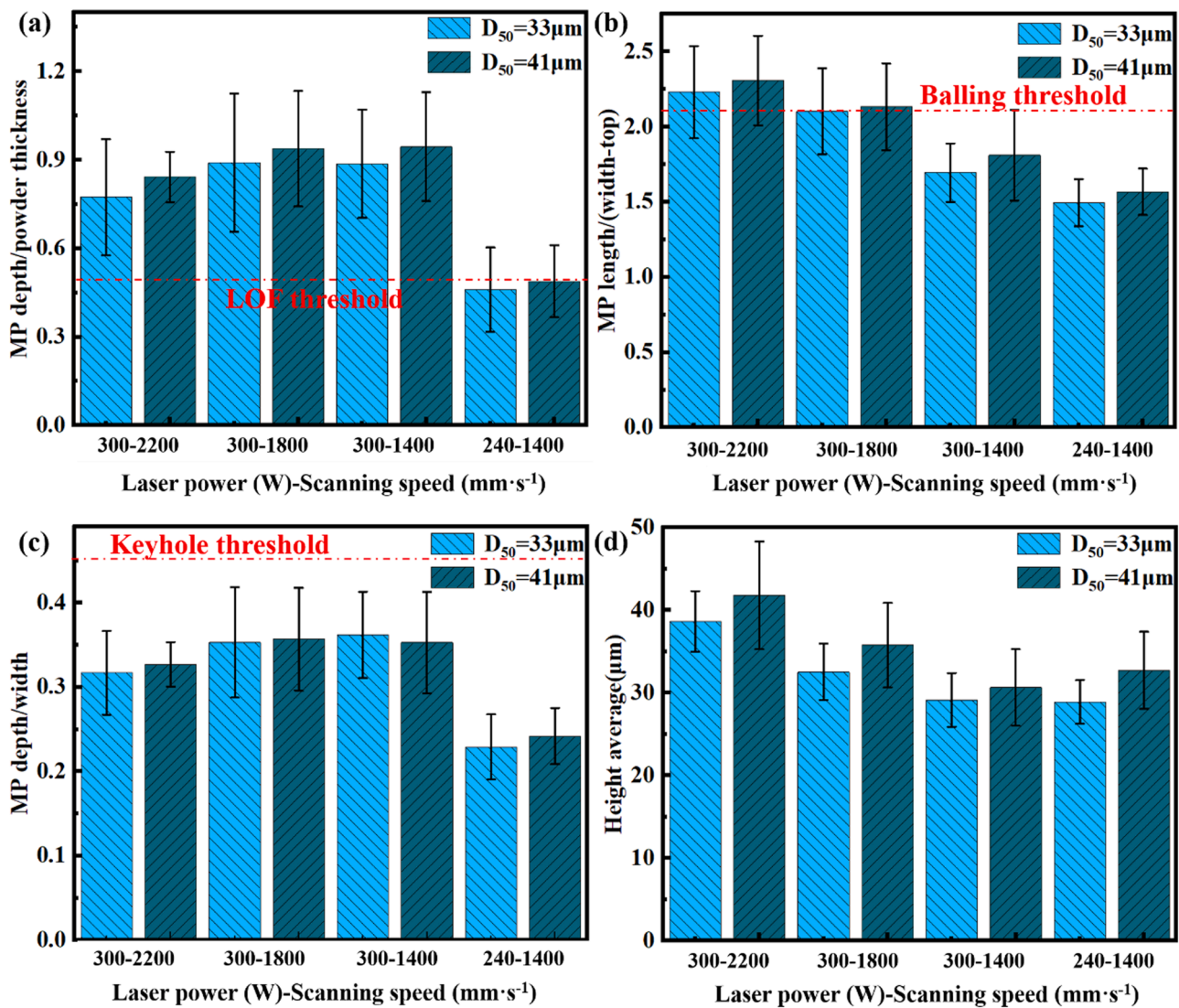
Fig. 6. The Effects of different powder sizes on the molten pool characteristics and solidified track height with D_{50} = 33 μm and 41 μm, respectively, (a) ratio of molten pool depth to powder thickness, (b) ratio of molten pool length to width, (c) ratio of molten pool depth to width, (d) solidified track height.
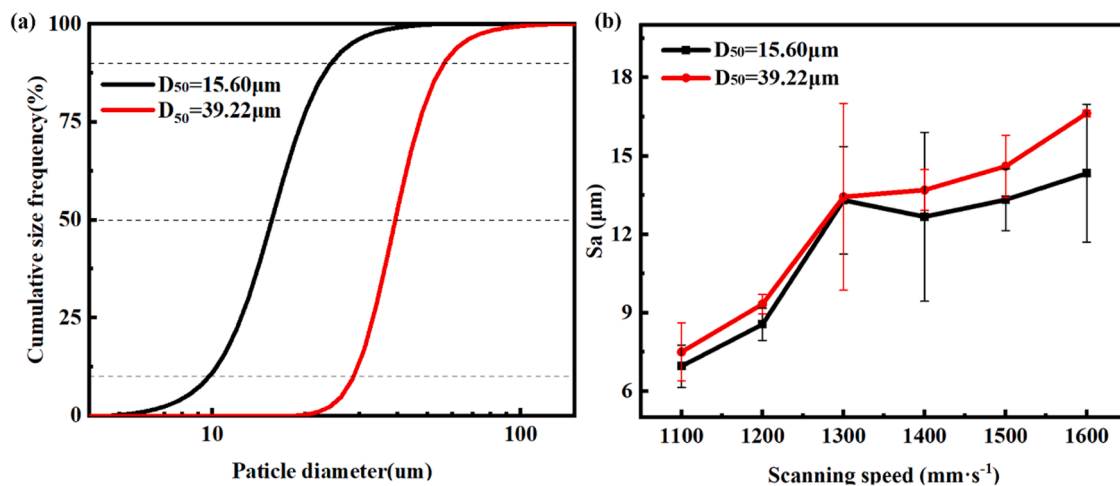

Fig. 7. The effects of powder sizes on the surface roughness in single layer experiments, (a) distribution of two kinds of powder size, with D_{50} = 15.60 μm and 39.22 μm, respectively. (b) Effects of different scanning speed on the surface roughness with the laser power 240 W.
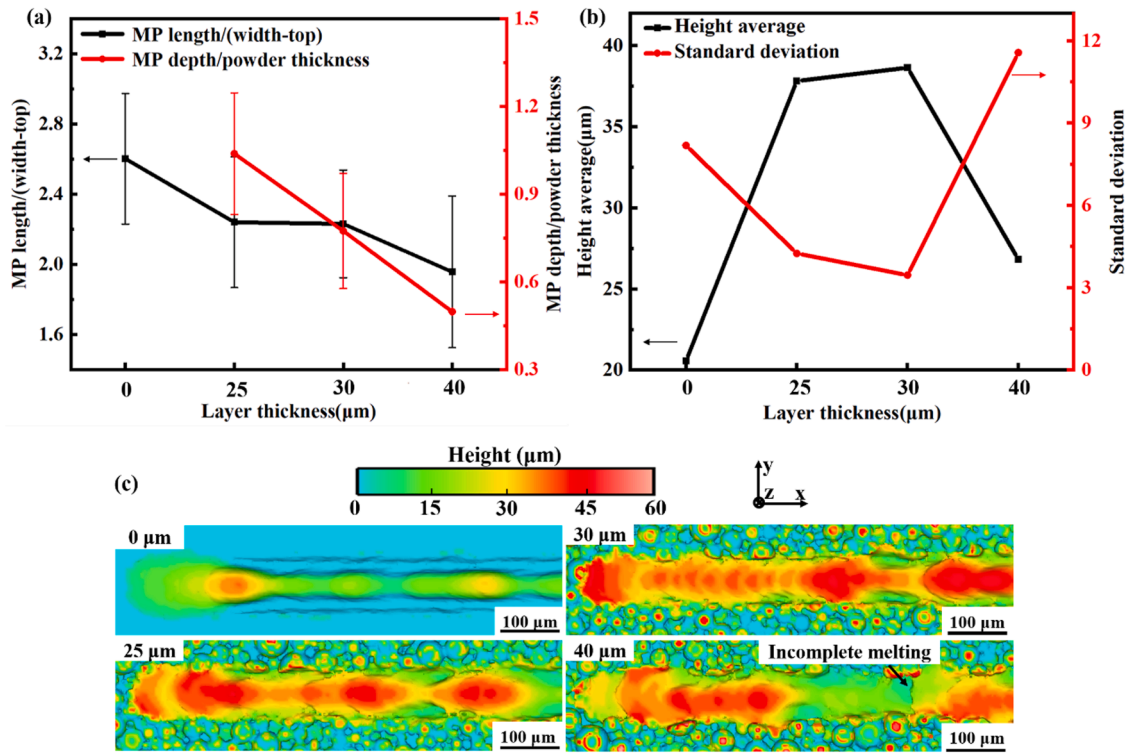
Fig. 8. Effects of layer thickness on the (a) ratio of molten pool length/width and ratio of depth/powder thickness, (b) solidified track height and (c) track-height color map from the top view with a laser power of 300 W and scanning speed of 2200 mm·s^{-1}. The number in the upper left in (c) shows the powder layer thickness.

mechanistic variables can be done via the Pearson correlation coefficient, which is used in statistics to measure the linear correlation of two variables. Six mechanistic variables are selected based on wide knowledge on metallurgy and mechanisms of various phenomena [42–45]. The Pearson correlation analysis (Fig. 9) shows that Ma and Tp has a strong correlation, which is up to 94%, and the correlation between Ma and the fr also reaches 87%. Thus, Ma is discarded and other five variables are used for the machine learning analysis. Although the largest correlation (Tp and fr) in the remaining variables also reaches 78%, in the analysis of small sample data, it will just enhance the redundancy. Therefore, it is considered reasonable given that these two variables are important for the analysis of molten pool dynamics, similar analytical variables are used in relevant literature [43].

This is a multi-classification problem, including LOF, balling, good and keyhole. The built quality for different printing parameters is classified based on the molten pool morphology. Five mechanistic variables are computed via a multi-physics model, and then applied to different machine learning methods to establish the correlation between the built quality and the mechanistic variables, and to predict the built quality for given printing parameters. A decision tree is constructed to predict built

quality based on the calculated mechanistic variables (Fig. 10). For any given printing parameters, the classification can be made by comparing the values of the mechanistic variables with the thresholds at each node. The decision starts from Fo, which is determined by the Gini index, and continues by checking the values of other variables until a final decision is made on the classification. The resulting prediction is proved to be accurate by the confusion matrix in Fig. 11(a), in which the accuracy is up to 0.862. Despite that the decision tree provides a visual tool to predict the built quality, there is no quantitative correlations between these five mechanistic variables and the final built quality. These correlations can provide guidance for adjusting the variables in quality monitoring. Poly-support vector machine can provide an algebraic equation of a hyperplane, which contains five mechanistic variables. For a given printing parameter, the corresponding quality classification can be obtained by substituting the computed five mechanistic variable values. However, the multiple classification corresponding to different values of the five mechanistic variables makes the equation of the hyperplane cumbersome. Moreover, the presence of five input variables hinders the visual representation of the hyperplane.

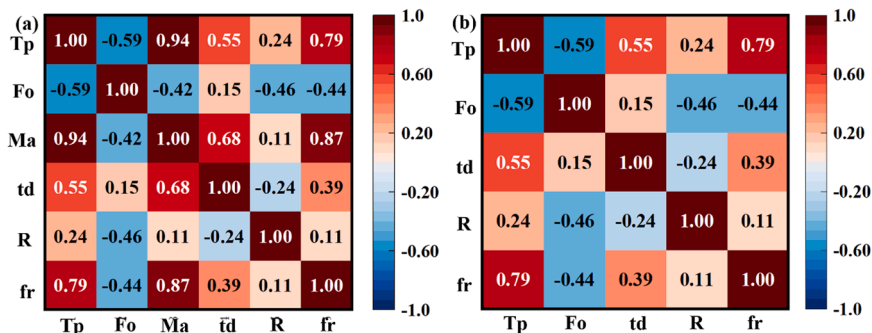The equations can be obtained by logistic regression model to con-

Fig. 9. Pearson matrixes of the (a) six and (b) five mechanistic variables to show the correlation coefficient.
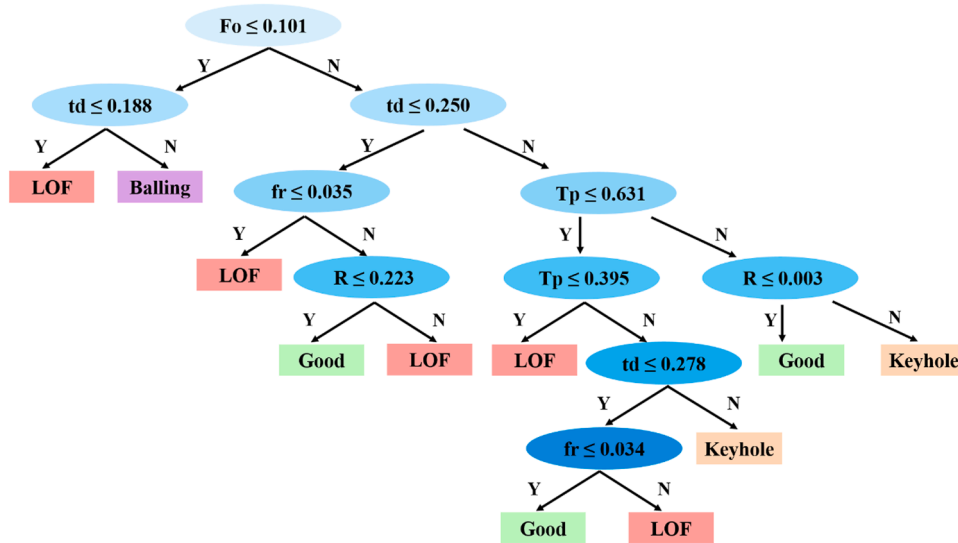
Fig. 10. A decision tree constructed based on the normalized values of the five mechanistic variables to predict the built quality.
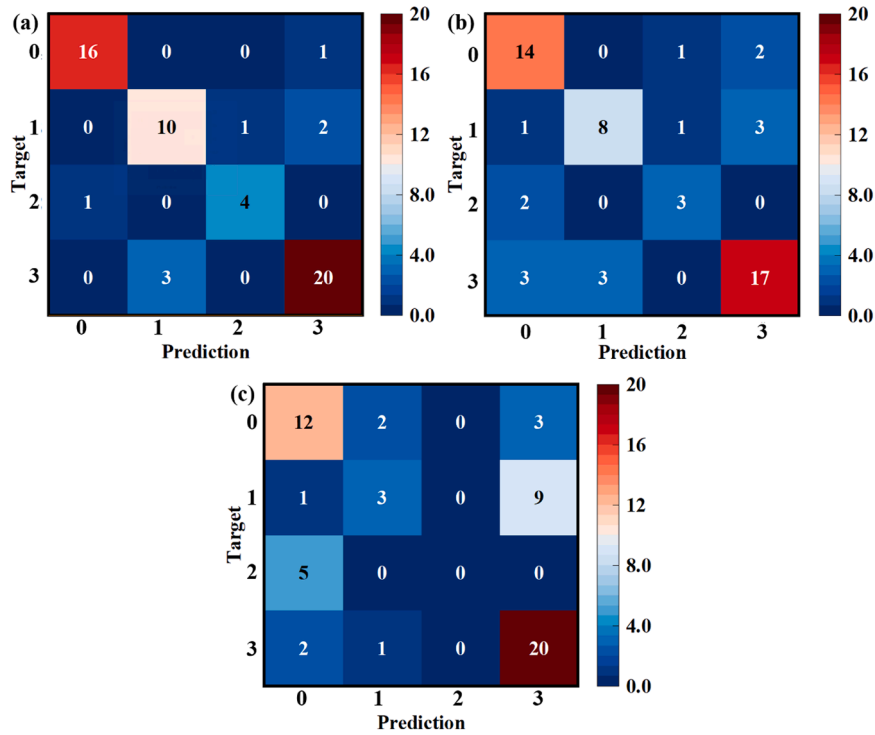

Fig. 11. Confusion matrixes of different machine learning methods to predict the built quality, (a) decision tree, (b) poly-support vector machine and (c) logistic regression.

nect the five mechanistic variables and different phenomena. The data fitting with Sigmoid function is used to predict the built quality. For a given printing parameter combination, the built quality prediction (QPI, quality prediction index) can be determined by:

$$QPI = \max\left(\frac{1}{1 + e^{-y_i}}\right) i = B, \ G, \ K, \ L \tag{13}$$

$$y_B = -0.375Tp - 0.76Fo - 2.425 \times 10^{-4}R - 4.606 \times 10^{-5}td + 0.112fr$$
$$- 0.0341 \tag{14}$$

$$y_G = 1.274Tp + 0.763Fo + 2.898 \times 10^{-4}R - 6.022 \times 10^{-5}td - 0.107fr$$
$$- 2.818 \tag{15}$$

$$y_K = 0.372Tp + 0.260Fo + 2.327 \times 10^{-4}R - 4.138 \times 10^{-6}td + 7.716fr$$
$$- 3.123 \tag{16}$$

$$y_L = -1.27Tp - 0.264Fo - 2.8 \times 10^{-4}R + 1.104 \times 10^{-4}td - 8.188e - 2fr + 5.975$$

(17)

in which Tp, Fo, R, td and fr represent the dimensionless peak temperature, Fourier number, Richardson number, solidification time (s) and the ratio of recoil pressure and surface tension. The detailed prediction procedure is to obtain the y_i values corresponding to the four phenomena by substituting five computed mechanistic variables into Eqs. (14-17). Then, the four y_i values are introduced into the Sigmoid function, and the predicted result is the phenomenon corresponding to the largest function value. However, the prediction accuracy of 60.3% is the lowest among the 3 classification algorithms (Fig. 11 and Table 2).

3.3. Hierarchical influence of the mechanistic variables

The comparative influence of the five mechanistic variables on the built quality can be determined by the coefficients in the fitting equations by logistic regression, which can be concluded from the Sigmoid function that the coefficients of each variable are proportional to the probability of the corresponding phenomenon occurrence. Positive coefficients indicate that the variables promote the corresponding phenomenon, while negative values indicate the opposite effect, which will decrease the phenomenon susceptibility with higher variable values. It can be seen from Fig. 12 that Tp, Fo and fr are very important to the built quality, ranking in the top three of the five variables. But for each phenomenon, the most important factors are different. For balling, Fo is the most important factor, followed by Tp and fr. The Fo indicates the ability of thermal disturbance to propagate deeply into the interior in an unsteady process, and a larger value means greater thermal disturbance, implying that the thermal disturbance in the molten pool plays a major role in the occurrence of balling, which in turn also uncovers that the balling physics is closely related to the disturbance in the molten pool. For the good phenomenon, the most important factor is found to be Tp, followed by the Fo and fr, indicating that reasonable heat combined with moderate thermal disturbance in the molten pool, will promote the fluid diffusing evenly, and lead to better printing quality. In the case of keyhole phenomenon, fr is the most important factor, indicating that keyhole is mainly controlled by the competition between the recoil pressure and surface tension. It appears when recoil pressure prevails and splits the free surface of molten pool as the recoil pressure promotes the keyhole opening while surface tension maintains the integrity of the molten pool upper surface. In addition, Tp is also very important due to the fact that keyhole only forms if the temperature exceeds the boiling point and evaporate intensively. Tp is the most important factor for LOF defects, which is the manifestation of insufficient heat input and suggests that increasing the heat absorption by the molten pool can reduce the LOF defects, for example preheating, larger power and small scanning speed. As the mechanistic variable values are the comprehensive results of multiple processing parameters, this hierarchy importance also provides new insights into the process optimization not just

adjusting the power and scanning speed.

The hierarchy importance of the five mechanistic variables can also be determined by three classification indices, including information gain, information gain ratio and Gini index (Fig. 13). The information gain and gain ratio values for the fr and Fo rank the top two, indicating the importance of these two variables in built quality. The Gini values for these two variables is at the bottom of the ranking, which further identifies them as the most important contribution to printing quality. Relatively speaking, R has the least influence. These results are consistent with the order of importance based on the logistic regression equation, and the comparison of the influence of each variable on the quality is helpful to select the appropriate variable value and obtain a good built quality.

4. Conclusions

In this work, a comprehensive framework containing high-fidelity powder-scale mechanistic model and physics-informed machine learning is established to predict the built quality and to determine the hierarchy importance of mechanistic variables for different built qualities in a multi-classification problem in the processing space. The major findings are as follows:

1. Preheating has an influence on the molten pool characteristics and solidified track quality. For the LOF defects, reasonable preheating temperature lowers the LOF voids and obtains smoother surface. While for the balling defects, preheating promotes the surface fluctuations.
2. The simulated results indicate that a higher surface roughness is obtained when the average powder size increases from 33 μm to 41 μm, and similar results are observed in experiments. The surface quality can be improved by using small size powder with reasonable heat input.
3. A thicker powder bed will lower the heat transfer efficient, increasing the vulnerability to LOF defects.
4. Five mechanistic variables are determined by Pearson correlation for the analysis of the physical mechanism of different phenomena, including dimensionless peak temperature, Fourier number, Richardson number, solidification time and the ratio of recoil pressure and surface tension. A decision tree is constructed and an index of QPI connecting the five variables and the built quality is established, which can realize the prediction for given printing parameters.
5. The hierarchy importance of the mechanistic variables is determined by the QPI and three machine learning inductions. Fo ranks first for balling phenomenon, implying that thermal disturbance in the molten pool plays a dominate role in balling formation. For the good built quality, the most important factor is Tp, followed by Fo and fr, suggesting that reasonable heat absorption combined with moderate thermal disturbance promoting the better printing quality. The top ranking of fr for keyhole phenomenon indicates that keyhole is mainly controlled by the competition between the recoil pressure and surface tension. Tp is the most important factor of LOF defects, meaning that increasing the heat absorption can reduce the LOF defects, for example preheating. As the mechanistic variable values are the comprehensive results of multiple processing parameters, this hierarchy ranking not only deepens the scientific understanding of different phenomenology, but also provides new insights and strategies for the process optimization.

CRediT authorship contribution statement

Liping Guo: Software, Data curation, Formal analysis, Investigation, Writing – original draft. **Hanjie Liu:** Data curation, Writing – original draft, Writing – review & editing. **Hongze Wang:** Conceptualization, Methodology, Writing – original draft, Writing – review & editing,
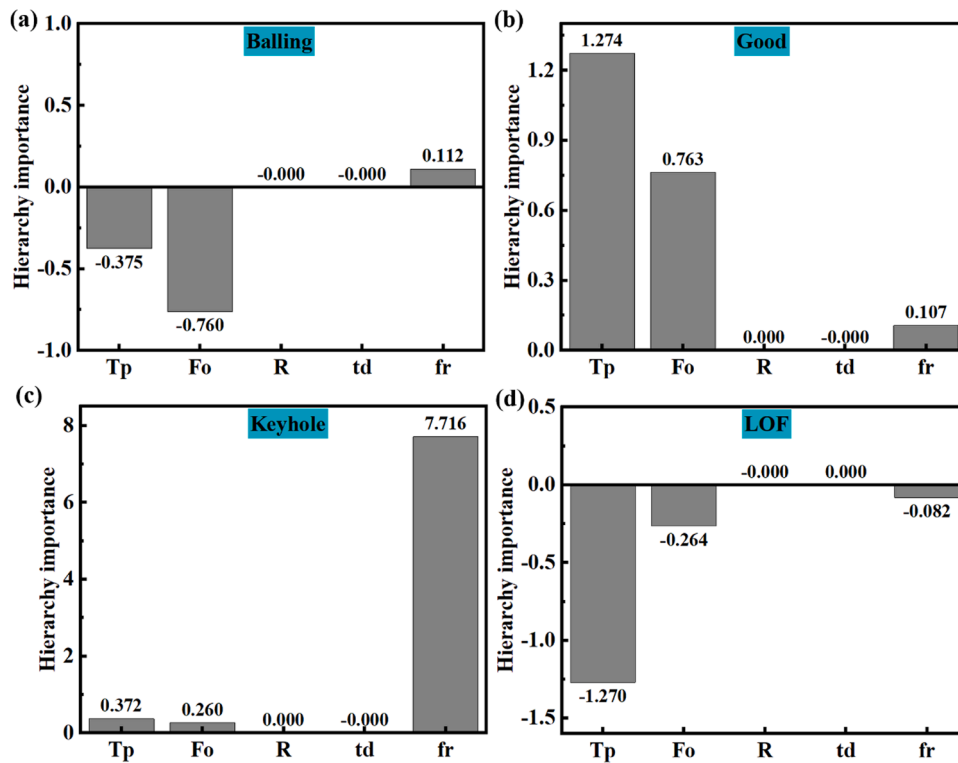
Table 2
Prediction accuracy, precision, recall and macro-F1 values of different machine learning methods. Accuracy is the ratio of correct predictions to the total predictions. Precision (Pre) is the ratio of predicted positive to the true positive of all the data. Recall (Rec) represents the proportion of correctly predicted positive to the true positive of all the data. $F1 = \dfrac{2 \times Pre \times Rec}{Pre + Rec}$. 'Macro' indicates that the corresponding indicator is an average value, giving all categories the same weight.

	Accuracy	Precision	Recall	Macro-F1
DT	0.862	0.845	0.845	0.845
SVM	0.724	0.700	0.690	0.695
LR	0.603	0.430	0.450	0.423

Fig. 12. Hierarchy importance of the five mechanistic variables determined by the coefficients in the logistic regression equation for (a) balling, (b) good, (c) keyhole and (d) LOF.
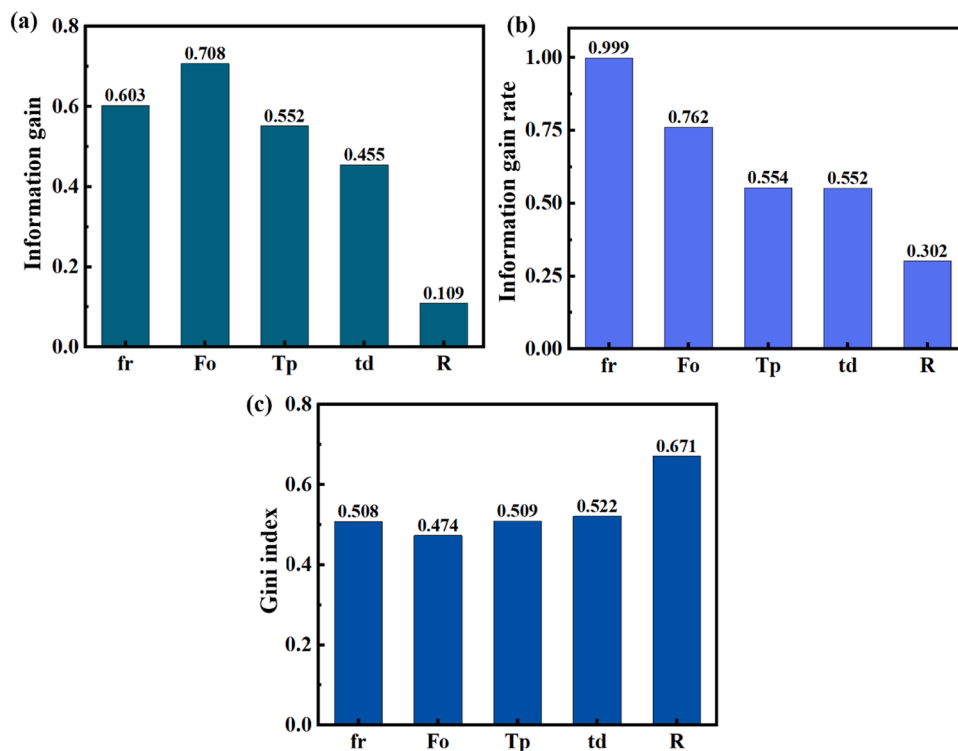

Fig. 13. Hierarchy importance of the five mechanistic variables determined by (a) information gain, (b) information gain ratio and (c) Gini index.

Declaration of Competing Interest

The authors declare that they have no known competing financial interests or personal relationships that could have appeared to influence

the work reported in this paper.

Data availability

Data will be made available on request.

Acknowledgments

Supplementary materials

Supplementary material associated with this article can be found, in the online version, at doi:10.1016/j.ijheatmasstransfer.2023.124596.

References

[1] X. Li, Q. Guo, L. Chen, W. Tan, Quantitative investigation of gas flow, powder-gas interaction, and powder behavior under different ambient pressure levels in laser powder bed fusion, Int. J. Mach. Tool. Manu. 170 (2021), 103797.

[2] B.K. Panda, S. Sahoo, Thermo-mechanical modeling and validation of stress field during laser powder bed fusion of AlSi10Mg built part, Result. Phys. 12 (2019) 1372–1381.

[3] L. Wang, Y. Zhang, H.Y. Chia, W. Yan, Mechanism of keyhole pore formation in metal additive manufacturing, npj Comput. Mater. 8 (2022) 22.

[4] L.P. Guo, Q.L. Wei, H.Z. Wang, H.J. Liu, A comprehensive model to quantify the effects of additional nano-particles on the printability in laser powder bed fusion of aluminum alloy and composite, Addit. Manuf. 58 (2022), 103011.

[5] I. Bitharas, N. Parab, C. Zhao, T. Sun, A.D. Rollett, A.J. Moore, The interplay between vapour, liquid, and solid phases in laser powder bed fusion, Nat. Commun. 13 (2022) 2959.

[6] L. Johnson, M. Mahmoudi, B. Zhang, R. Seede, X. Huang, J.T. Maier, H.J. Maier, I. Karaman, A. Elwany, R. Arróyave, Assessing printability maps in additive manufacturing of metal alloys, Acta Mater 176 (2019) 199–210.

[7] T.H.C. Childs, C. Hauser, M. Badrossamay, Selective laser sintering (melting) of stainless and tool steel powders: experiments and modelling, P. I. Mech. Eng. B-J. Eng. 219 (2006) 339–357.

[8] J.H. Martin, B.D. Yahata, J.M. Hundley, J.A. Mayer, T.A. Schaedler, T.M. Pollock, 3D printing of high-strength aluminium alloys, Nature 549 (2017) 365–369.

[9] M.L. Qu, Q.L. Guo, L.I. Escano, A. Nabaa, K. Fezzaa, L.Y. Chen, Nanoparticle-enabled increase of energy efficiency during laser metal additive manufacturing, Addit. Manuf. 60 (2022), 103242.

[10] M.L. Qu, Q.L. Guo, L.I. Escano, J.D. Yuan, S.M.H. Hojjatzadeh, S.J. Clark, K. Fezzaa, T. Sun, L.Y. Chen, Controlling melt flow by nanoparticles to eliminate surface wave induced surface fluctuation, Addit. Manuf. 59 (2022), 103081.

[11] M.L. Qu, Q.L. Guo, L.I. Escano, A. Nabaa, S.M.H. Hojjatzadeh, Z.A. Young, L. Y. Chen, Controlling process instability for defect lean metal additive manufacturing, Nat. Commun. 13 (2022) 1079.

[12] D. Tomus, P.A. Rometsch, M. Heilmaier, X. Wu, Effect of minor alloying elements on crack-formation characteristics of Hastelloy-X manufactured by selective laser melting, Addit. Manuf. 16 (2017) 65–72.

[13] M.J. Matthews, G. Guss, S.A. Khairallah, A.M. Rubenchik, P.J. Depond, W.E. King, Denudation of metal powder layers in laser powder bed fusion processes, Acta Mater 114 (2016) 33–42.

[14] Q.L. Guo, C. Zhao, L.I. Escano, Z. Young, L.H. Xiong, K. Fezzaa, W. Everhart, B. Brown, T. Sun, L.Y. Chen, Transient dynamics of powder spattering in laser powder bed fusion additive manufacturing process revealed by in-situ high-speed high-energy x-ray imaging, Acta Mater. 151 (2018) 169–180.

[15] W.H. Wang, W.H. Lin, R. Yang, Y.N. Wu, J. Li, Z.B. Zhang, Z.R. Zhai, Mesoscopic evolution of molten pool during selective laser melting of superalloy Inconel 738 at elevating preheating temperature, Mater. Design 213 (2022) 110355.

[16] Z. Wu, M. Asherloo, R. Jiang, M.H. Delpazir, N. Sivakumar, M. Paliwal, J. Capone, B. Gould, A. Rollett, A. Mostafaei, Study of printability and porosity formation in laser powder bed fusion built hydride-dehydride (HDH) Ti-6Al-4 V, Addit. Manuf. 47 (2021), 102323.

[17] U.S. Bertoli, A.J. Wolfer, M.J. Matthews, J.-P.R. Delplanque, J.M. Schoenung, On the limitations of volumetric energy density as a design parameter for selective laser melting, Mater. Des. 113 (2017) 331–340.

[18] W. Yan, W. Ge, Y. Qian, S. Lin, B. Zhou, W.K. Liu, F. Lin, G.J. Wagner, Multi-physics modeling of single/multiple-track defect mechanisms in electron beam selective melting, Acta Mater. 134 (2017) 324–333.

[19] P. Zagade, B.P. Gautham, A. De, T. DebRoy, Analytical estimation of fusion zone dimensions and cooling rates in part scale laser powder bed fusion, Addit. Manuf. 46 (2021).

[20] C. Panwisawas, C. Qiu, M.J. Anderson, Y. Sovani, R.P. Turner, M.M. Attallah, J. W. Brooks, H.C. Basoalto, Mesoscale modelling of selective laser melting: thermal fluid dynamics and microstructural evolution, Comp. Mater. Sci. 126 (2017) 479–490.

[21] G.R. Nazami, S. Sahoo, Influence of hatch spacing and laser spot overlapping on heat transfer during laser powder bed fusion of aluminum alloy, J Laser Appl 32 (2020).

[22] S.A. Khairallah, A.T. Anderson, A. Rubenchik, W.E. King, Laser powder-bed fusion additive manufacturing: physics of complex melt flow and formation mechanisms of pores, spatter, and denudation zones, Acta Mater. 108 (2016) 36–45.

[23] S.M.H. Hojjatzadeh, N.D. Parab, W. Yan, Q. Guo, L. Xiong, C. Zhao, M. Qu, L. I. Escano, X. Xiao, K. Fezzaa, W. Everhart, T. Sun, L. Chen, Pore elimination mechanisms during 3D printing of metals, Nat. Commun. 10 (2019) 3088.

[24] T. Yu, J.D. Zhao, Quantitative simulation of selective laser melting of metals enabled by new high-fidelity multiphase, multiphysics computational tool, Comput. Method. Appl. M. 399 (2022), 115422.

[25] C.L.A. Leung, D. Luczyniec, E. Guo, S. Marussi, R.C. Atwood, M. Meisnar, B. Saunders, P.D. Lee, Quantification of interdependent dynamics during laser additive manufacturing using X-ray imaging informed multi-physics and multiphase simulation, Adv. Sci. 9 (2022), 2203546.

[26] Y. Huang, T.G. Fleming, S.J. Clark, S. Marussi, K. Fezzaa, J. Thiyagalingam, C.L. A. Leung, P.D. Lee, Keyhole fluctuation and pore formation mechanisms during laser powder bed fusion additive manufacturing, Nat. Commun. 13 (2022) 1170.

[27] Y. Chen, H. Wang, Y. Wu, H. Wang, Predicting the printability in selective laser melting with a supervised machine learning method, Mater. (Basel) 13 (2020) 5063.

[28] R. Seede, D. Shoukr, B. Zhang, A. Whitt, S. Gibbons, P. Flater, A. Elwany, R. Arroyave, I. Karaman, An ultra-high strength martensitic steel fabricated using selective laser melting additive manufacturing: densification, microstructure, and mechanical properties, Acta Mater. 186 (2020) 199–214.

[29] L. Scime, J. Beuth, Using machine learning to identify in-situ melt pool signatures indicative of flaw formation in a laser powder bed fusion additive manufacturing process, Addit. Manuf. 25 (2019) 151–165.

[30] C. Zhao, N.D. Parab, X. Li, K. Fezzaa, W. Tan, A.D. Rollett, T. Sun, Critical instability at moving keyhole tip generates porosity in laser melting, Science 370 (2020) 1080–1086.

[31] C.L.A. Leung, S. Marussi, R.C. Atwood, M. Towrie, P.J. Withers, P.D. Lee, In situ X-ray imaging of defect and molten pool dynamics in laser additive manufacturing, Nat. Commun. 9 (2018) 1355.

[32] R. Cunningham, C. Zhao, N. Parab, C. Kantzos, J. Pauza, K. Fezzaa, T. Sun, A. D. Rollett, Keyhole threshold and morphology in laser melting revealed by ultrahigh-speed X-ray imaging, Science 363 (2019) 849–852.

[33] A.A. Martin, N.P. Calta, J.A. Hammons, S.A. Khairallah, M.H. Nielsen, R. M. Shuttlesworth, N. Sinclair, M.J. Matthews, J.R. Jeffries, T.M. Willey, J.R.I. Lee, Ultrafast dynamics of laser-metal interactions in additive manufacturing alloys captured by in situ X-ray imaging, Mater. Today Adv. 1 (2019), 100002.

[34] J. Jakumeit, G. Zheng, R. Laqua, S.J. Clark, J. Zielinski, J.H. Schleifenbaum, P. D. Lee, Modelling the complex evaporated gas flow and its impact on particle spattering during laser powder bed fusion, Addit. Manuf. 47 (2021), 102332.

[35] S.A. Khairallah, A.A. Martin, J.R.I. Lee, G. Guss, N.P. Calta, Controlling interdependent meso-nanosecond dynamics and defect generation in metal 3D printing, Science 368 (2020) 660–665.

[36] M. Samantaray, S. Sahoo, D. Thatoi, Modeling of thermal and solidification behavior during laser additive manufacturing of AlSi10Mg alloy powders and its experimental validation, J Laser Appl 31 (2019).

[37] M. Samantaray, D. Nath Thatoi, S. Sahoo, Finite element simulation of heat transfer in laser additive manufacturing of AlSi10Mg powders, Mater. Today: Proceed. 22 (2020) 3001–3008.

[38] D. Wu, X. Hua, Y. Ye, L. Huang, F. Li, Y. Huang, Experimental and numerical study of spatter formation and composition change in fiber laser welding of aluminum alloy, J. Phys. D: Appl. Phys. 51 (2018), 185604.

[39] E.L. Papazoglou, N.E. Karkalos, A.P. Markopoulos, A comprehensive study on thermal modeling of SLM process under conduction mode using FEM, Int. J. Adv. Manuf. Tech. 111 (2020) 2939–2955.

[40] C. Panwisawas, Y. Gong, Y.T. Tang, R.C. Reed, J. Shinjo, Additive manufacturability of superalloys: process-induced porosity, cooling rate and metal vapour, Addit. Manuf. 47 (2021), 102339.

[41] B. Mondal, T. Mukherjee, T. DebRoy, Crack free metal printing using physics informed machine learning, Acta Mater. 226 (2022) 117612.

[42] M. Jiang, T. Mukherjee, Y. Du, T. DebRoy, Superior printed parts using history and augmented machine learning, npj Comput. Mater. 8 (2022) 10.

[43] Y. Du, T. Mukherjee, T. DebRoy, Physics-informed machine learning and mechanistic modeling of additive manufacturing to reduce defects, Appl. Mater. Today 24 (2021) 101123.

[44] Y. Du, T. Mukherjee, P. Mitra, T. DebRoy, Machine learning based hierarchy of causative variables for tool failure in friction stir welding, Acta Mater. 192 (2020) 67–77.

[45] Q. Wu, T. Mukherjee, A. De, T. DebRoy, Residual stresses in wire-arc additive manufacturing – Hierarchy of influential variables, Addit. Manuf. 35 (2020), 101355.

[46] Y. Du, T. Mukherjee, T. DebRoy, Conditions for void formation in friction stir welding from machine learning, npj Comput. Mater. 5 (2019) 68.

[47] L. Sinclair, C.L.A. Leung, S. Marussi, S.J. Clark, Y. Chen, M.P. Olbinado, A. Rack, J. Gardy, G.J. Baxter, P.D. Lee, In situ radiographic and ex situ tomographic analysis of pore interactions during multilayer builds in laser powder bed fusion, Addit. Manuf. 36 (2020), 101512.

[48] E.W. Jost, J.C. Miers, A. Robbins, D.G. Moore, C. Saldana, Effects of spatial energy distribution-induced porosity on mechanical properties of laser powder bed fusion 316 L stainless steel, Addit. Manuf. 39 (2021), 101875.

[49] C. Tang, K.Q. Le, C.H. Wong, Physics of humping formation in laser powder bed fusion, Int. J. Heat Mass Transfer 149 (2020), 119172.

[50] Y.S. Lee, W. Zhang, Mesoscopic simulation of heat transfer and fluid flow in laser powder bed additive manufacturing, in: 26th Solid Freeform Fabrication Symposium, Austin, Texas, 2015, pp. 1154–1165.

[51] S.M.H. Hojjatzadeh, N.D. Parab, Q.L. Guo, M.L. Qu, L.H. Xiong, C. Zhao, L. I. Escano, K. Fezzaa, W. Everhart, T. Sun, L.Y. Chen, Direct observation of pore formation mechanisms during LPBF additive manufacturing process and high energy density laser welding, Int. J. Mach. Tool. Manu. 153 (2020), 103555.

[52] T. Mukherjee, J.S. Zuback, A. De, T. DebRoy, Printability of alloys for additive manufacturing, Sci. Rep. 6 (2016) 19717.

[53] L. Guo, H. Wang, H. Liu, Y. Huang, Q. Wei, C.L.A. Leung, Y. Wu, H. Wang, Understanding keyhole induced-porosities in laser powder bed fusion of aluminum and elimination strategy, Int. J. Mach. Tool. Manu. 184 (2023), 103977.

[54] S.A. Khairallah, T. Sun, B.J. Simonds, Onset of periodic oscillations as a precursor of a transition to pore-generating turbulence in laser melting, Addit. Manuf. Lett. 1 (2021), 100002.

[55] A.A. Martin, N.P. Calta, S.A. Khairallah, J. Wang, P.J. Depond, A.Y. Fong, V. Thampy, G.M. Guss, A.M. Kiss, K.H. Stone, C.J. Tassone, J.N. Weker, M. F. Toney, T. van Buuren, M.J. Matthews, Dynamics of pore formation during laser powder bed fusion additive manufacturing, Nat. Commun. 10 (2019) 1987.

[56] Y.K. Xiao, Z.Y. Bian, Y. Wu, G. Ji, Y.Q. Li, M.J. Li, Q. Lian, Z. Chen, A. Addad, H. W. Wang, Effect of nano-TiB2 particles on the anisotropy in an AlSi10Mg alloy processed by selective laser melting, J. Alloys Compd. 798 (2019) 644–655.

[57] J. Zhang, D. Gu, Y. Yang, H. Zhang, H. Chen, D. Dai, K. Lin, Influence of particle size on laser absorption and scanning track formation mechanisms of pure tungsten powder during selective laser melting, Engineering 5 (2019) 736–745.

[58] D. Gu, Y. Yang, L. Xi, J. Yang, M. Xia, Laser absorption behavior of randomly packed powder-bed during selective laser melting of SiC and TiB2 reinforced Al matrix composites, Opt. Laser Technol. 119 (2019), 105600.

[59] J. Nandy, H. Sarangi, S. Sahoo, A review on direct metal laser sintering: process features and microstructure modeling, Laser. Manufact. Mater. Process. 6 (2019) 280–316.

[60] S. Sahoo, Direct metal laser sintering of AlSi10Mg alloy parts: modeling of temperature profile, Mater. Today: Proceed. 35 (2021) 118–123.